Excitation of Low-Frequency QPOs in Black-Hole Accretion Flows

Mami MACHIDA

Division of Theoretical Astronomy, National Astronomical Observatory of Japan,
2–21–1 Osawa, Mitaka-shi, Tokyo 181–8588
mami@th.nao.ac.jp
and
Ryoji MATSUMOTO

Department of Physics, Faculty of Science, Chiba University, 1-33 Yayoi-cho, Inage-ku, Chiba 263-8522
matumoto@astro.s.chiba-u.ac.jp

Abstract

We present the results of global three-dimensional magneto-hydrodynamic simulations of black-hole accretion flows. We focus on the dependence of the numerical results on the gas temperature supplied from the outer region. General-relativistic effects were taken into account using the pseudo-Newtonian potential. We ignored radiative cooling of the accreting gas. The initial state was a torus threaded by a weak azimuthal magnetic field. We found that the mass-accretion rate and the mass-outflow rate strongly depend on the temperature of the initial torus. The ratio of the average Maxwell stress generated by the magneto-rotational instability (MRI) to the gas pressure, $\alpha \equiv \langle B_\varpi B_\varphi / 4\pi \rangle / \langle P \rangle$, is $\alpha \sim 0.05$ in a hot torus and $\alpha \sim 0.01$ in a cool torus. In the cool model, a constant angular momentum inner torus is formed around 4–$8\,r_s$, where r_s is the Schwarzschild radius. This inner torus deforms itself from a circle to a crescent quasi-periodically. During this deformation, the mass-accretion rate, the magnetic energy and the Maxwell stress increase. As the magnetic energy is released, the inner torus returns to a circular shape and starts the next cycle.

The power spectral density (PSD) of the time variation of the mass-accretion rate in the cool model has a low-frequency peak around $10\,\mathrm{Hz}$ when we assumed a $10 M_\odot$ black hole. The mass outflow rate in the low temperature model also shows quasi-periodic oscillation.

Key words: accretion, accretion disks — black hole physics — dynamo — magnetohydrodynamics: MHD — QPO

1. Introduction

Accretion disks are believed to be the energy source of various activities in active galactic nuclei, X-ray binaries, protostars and so on. Using the RXTE satellite, a detailed timing analysis of X-ray binaries has been carried out (e.g., Homan et al. 2005; McClintock & Remillard 2006; Shaposhnikov et al. 2007). Black-hole candidates (BHCs) show transitions between a low/hard state (LHS) dominated by a hard power-law component and a high/soft state (HSS) characterized by a soft black body component. During the transition, BHCs stay in a hard intermediate state (HIMS) or in a soft intermediate state (SIMS) (Homan & Belloni 2005). The light curves during LHS of BHCs are subject to violent X-ray fluctuations, and sometimes accompany quasi-periodic oscillations (QPO) in the Fourier Power Spectral Density (PSD). The LHS is associated with steady outflows (e.g., Gallo et al. 2003). In this state, mass accretes to the black hole as an optically thin, advection-dominated accretion flow (e.g., Ichimaru 1977; Narayan & Yi 1994, 1995). The energy spectrum of the HIMS is softer than that in the LHS. Low-frequency (1–10 Hz) QPOs are observed in the luminous hard state and in the intermediate state (McClintock & Remillard 2006). High-frequency QPOs (~ 100 Hz) are sometimes observed in these states. The frequency of low-frequency QPOs in the

intermediate state moves to higher frequency and the low-frequency QPOs disappear when the state changes to HSS (see Belloni et al. 2006).

These observations indicate that QPOs are associated with cooling of the disk. By carrying out global three-dimensional (3D) magneto-hydrodynamic (MHD) simulations including radiative cooling, Machida et al. (2006) showed that when the accretion rate exceeds the limit for the onset of the cooling instability, the radiatively inefficient, optically thin disk transitions into a magnetically supported, cool, intermediate state. Oda et al. (2007) constructed a steady model of such disks and showed that their luminosity can exceed $0.1 L_{\mathrm{Edd}}$, where L_{Edd} is the Eddington luminosity. When the transition to the cool disk takes place in the outer region, cool gas will be supplied to the inner region.

Low-frequency QPOs are sometimes attributed to oscillation at the interface between the hot inner disk and the cool outer disk (e.g., Di Matteo & Psaltis 1999). The excitation mechanism of such an oscillation, however, was not clear. Another puzzle is the coexistence of low-frequency and high-frequency QPOs. Abramowicz and Kulźniak (2001) proposed that high-frequency QPOs are generated by the resonance between radial and vertical oscillations of accretion disks. Kato (2001a,b) pointed out that non-axisymmetric g-mode oscillations can be trapped in a thin, relativistic disk, and these oscillations are

excited by the corotation resonance. Non-linear couplings of disk oscillations and disk warp were examined by S. Kato (2004).

Y. Kato (2004) reproduced high-frequency QPOs by 3D MHD simulations of optically thin, geometrically thick accretion flows. They showed that the QPOs appear around the epicyclic frequency κ at $4r_s$ and $\Omega + \kappa$, where Ω is the Kepler frequency, and showed that the amplitudes of QPOs are damped after a while.

The $1/f$-noise-like fluctuations observed in BHCs have been reproduced by global 3D MHD simulations (e.g., Kawaguchi et al. 2000, Hawley 2001). Kawaguchi et al. (2000) showed that the PSD changes its slope at around 10 Hz when they assumed a $10M_\odot$ black hole. Machida and Matsumoto (2003) pointed out that magnetic reconnection in the innermost region of the disk can be the origin of intermittent X-ray flares, known as X-ray shots (Negoro et al. 1995), which produce flat PSD at low frequency (~ 1 Hz).

In this paper, we report on the results of global 3D MHD simulations that produced low-frequency QPOs, and discuss their excitation mechanisms.

In section 2, we describe the basic equations and initial conditions. The results of simulations are given in section 3. In section 4, we concentrate on oscillation excited in the inner torus. Section 5 is devoted to discussion and conclusions.

2. Numerical Methods

2.1. Basic Equations

We solved the following resistive MHD equations in a cylindrical coordinate system (ϖ, φ, z):

$$\frac{\partial \rho}{\partial t} + \nabla \cdot (\rho \boldsymbol{v}) = 0 , \tag{1}$$

$$\rho \left[\frac{\partial \boldsymbol{v}}{\partial t} + \boldsymbol{v} \cdot \nabla \boldsymbol{v} \right] = -\nabla P - \rho \nabla \phi + \frac{\boldsymbol{j} \times \boldsymbol{B}}{c} , \tag{2}$$

$$\frac{\partial \boldsymbol{B}}{\partial t} = \nabla \times \left(\boldsymbol{v} \times \boldsymbol{B} - \frac{4\pi}{c} \eta \boldsymbol{j} \right) , \tag{3}$$

$$\rho T \frac{dS}{dt} = \frac{4\pi}{c^2} \eta j^2 , \tag{4}$$

where ρ, P, ϕ, $\boldsymbol{v}$, $\boldsymbol{B}$, $\boldsymbol{j} = c\nabla \times \boldsymbol{B}/4\pi$, η, T, and S are the density, pressure, gravitational potential, velocity, magnetic field, current density, resistivity, temperature and specific entropy, respectively. The specific entropy is expressed as $S = C_v \ln(P/\rho^\gamma)$, where C_v is the specific-heat capacity and γ is the specific-heat ratio. We included a Joule-heating term, but neglected a radiative-cooling term in the energy equation. We assumed an anomalous resistivity of $\eta = \eta_0 [\max(v_d/v_c - 1, 0)]^2$ (Yokoyama & Shibata 1994), where $v_d \equiv j/\rho$ is the electron–ion drift speed and v_c is the threshold above which anomalous resistivity sets in.

General-relativistic effects were simulated using the pseudo-Newtonian potential, $\phi = -GM/(r - r_s)$ (Paczyński & Wiita 1980), where G is the gravitational constant, M is the mass of the black hole, $r = (\varpi^2 + z^2)^{1/2}$, and r_s is the Schwarzschild radius. We neglected the self-gravity of the disk.

2.2. Numerical Methods and Boundary Conditions

We solved the resistive MHD equations using a modified Lax–Wendroff scheme (Rubin & Burstein 1967) with an artificial viscosity (Richtmyer & Morton 1967).

The units of length and velocity were the Schwarzschild radius r_s and the light speed c, respectively. The unit time was $t_0 = r_s c^{-1} = 10^{-4} M/10 M_\odot$ s. The unit temperature was given by $T_0 = m_p c^2 k_B^{-1} = 1.1 \times 10^{13}$ K, where m_p is the proton mass and k_B is the Boltzmann constant.

The number of grids was $(N_\varpi, N_\varphi, N_z) = (250, 64, 384)$. The grid size was $\Delta \varpi = \Delta z = 0.1$ for $0 < \varpi/r_s < 10$, and $|z|/r_s < 10$. For model LT (cool accretion disk), we set the grid interval as follows: $\Delta \varpi_n = \min(1.05\Delta \varpi_{n-1}, \Delta \varpi_{max})$, $\Delta z_n = \min(1.05\Delta z_{n-1}, \Delta z_{max})$, where $\Delta \varpi_{max} = 10 \Delta \varpi$ and $\Delta z_{max} = 10\Delta z$. The outer boundaries at $\varpi = 132 r_s$ and at $z = \pm 70 r_s$ were free boundaries, where waves can be transmitted. For model HT (hot accretion disk), we set $\Delta \varpi_{max} = 20\Delta \varpi$ and $\Delta z_{max} = 100\Delta z$. Therefore, the outer boundaries were located at $\varpi = 230 r_s$ and $z = \pm 170 r_s$, respectively. The grid size in the azimuthal direction was $\Delta \varphi = 2\pi/63$.

We included the full circle ($0 \le \varphi \le 2\pi$) in the simulation region, and applied periodic boundary conditions in the azimuthal direction. An absorbing boundary condition was imposed at $r = r_{in} = 2r_s$ by introducing a damping factor,

$$D = 0.1 \left(1 - \tanh \frac{r - r_{in} + 5\Delta \varpi}{2\Delta \varpi} \right) . \tag{5}$$

The physical quantities $q = (\rho, \boldsymbol{v}, \boldsymbol{B}, P)$ inside $r = r_{in}$ were re-evaluated by

$$q^{new} = q - D(q - q_0) , \tag{6}$$

which means that a deviation from the initial values, q_0, is artificially reduced with a damping rate of D. Waves propagating inside $r = r_{in}$ are absorbed in the transition region ($r_{in} - 5 \Delta \varpi < r < r_{in}$).

2.3. Initial Model

The initial state of our simulation was an equilibrium torus threaded by a weak toroidal magnetic field. At the initial state, the torus was assumed to have a specific angular momentum, $L \propto \varpi^a$.

The magnetic field distribution was determined according to Okada et al. (1989). We used the polytropic relation $P = K\rho^\gamma$ at the initial state and assumed

$$\beta = \frac{8\pi P}{B_\varphi^2} = \beta_b \left(\frac{\varpi}{\varpi_b} \right)^{-2(\gamma-1)} , \tag{7}$$

where β_b is the initial plasma β at the initial pressure maximum of the torus $(\varpi, z) = (\varpi_b, 0)$, and B_φ is the azimuthal magnetic field. We integrated the equation of motion into a potential form,

$$\Psi(\varpi, z) = \phi + \frac{L^2}{2\varpi^2} + \frac{1}{\gamma-1} v_s^2 + \frac{\gamma}{2(\gamma-1)} v_A^2 = \Psi_b$$
$$= \text{constant} , \tag{8}$$

where $v_s = (\gamma P/\rho)^{1/2}$ is the sound speed, $v_A = B_\varphi/(4\pi\rho)^{1/2}$ is the Alfvén speed, and $\Psi_b = \Psi(\varpi_b, 0)$. At $\varpi = \varpi_b$, the rotation
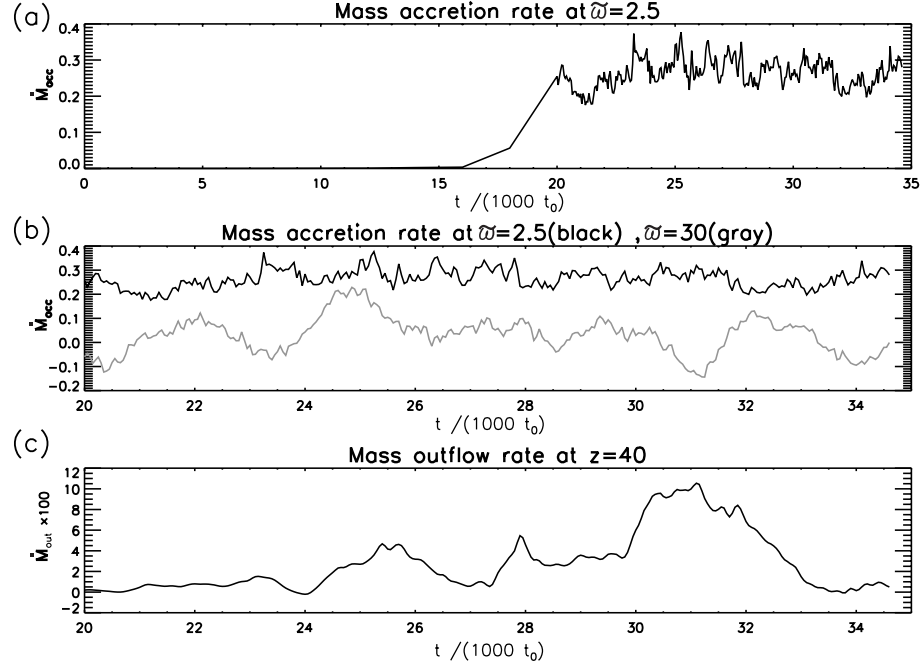
Fig. 1. (a) Time evolution of the mass-accretion rate for model HT measured at $\varpi = 2.5r_s$. (b)Time evolution of the mass-accretion rate at $\varpi = 2.5r_s$ (black) and $\varpi = 30r_s$ (gray). (c) Mass-outflow rate measured at $z = 40r_s$.

speed of the torus, L/ϖ_b, equals the Keplerian velocity. By using equation (8), we obtained the density distribution as

$$\rho = \rho_b \left\{ \frac{\max[\Psi_b - \phi - L^2/(2\varpi^2), 0]}{K[\gamma/(\gamma-1)][1 + \beta_b^{-1}\varpi^{2(\gamma-1)}/\varpi_b^{2(\gamma-1)}]} \right\}^{1/(\gamma-1)},$$
(9)

where ρ_b is the density at $(\varpi, z) = (\varpi_b, 0)$. Outside the torus, we assumed a hot, isothermal ($T = T_{halo}$) spherical halo. The density distribution of the halo is given by $\rho_h = \rho_{halo} \exp[-(\phi - \phi_b)/(k_B T_{halo})]$, where ϕ_b is the gravitational potential at $(\varpi, z) = (\varpi_b, 0)$.

In this paper, we report on the results of simulations for two models. Model HT assumes a hot outer torus with a sound speed of $c_b = 0.029c$ at $\varpi_b = 50r_s$. In model HT, the torus has a constant specific angular momentum ($a = 0$). Model LT is a cool disk model in which $c_b = 0.01c$ at $\varpi_b = 35r_s$ and $a = 0.43$. In both models, we adopted $\beta_b = 100$, $\gamma = 5/3$, $L = (\varpi_b/2)^{1/2}\varpi_b/(\varpi_b - 1)\varpi^a$, $\rho_{halo} = 10^{-4}\rho_b$, $\eta_0 = 5 \times 10^{-4}$, and $v_c = 0.9c$. Since we did not include radiative cooling, ρ_b was arbitrary. We adopted $\rho_b = 1$.

3. Numerical Results

3.1. A Hot Accretion Disk : Model HT

Figure 1a shows the time evolution of the mass-accretion rate for model HT measured at $\varpi = 2.5r_s$. Figure 1b shows the time evolution of the mass-accretion rate at $\varpi = 2.5r_s$ (black) and at $\varpi = 30r_s$ (gray). The mass-accretion rate $\dot{M}$ at $\varpi = 2.5r_s$ was computed by

$$\dot{M} = \int_{-20}^{20} \int_0^{2\pi} \rho \varpi v_\varpi \, d\varphi \, dz \ .$$
(10)

The mass accretion rate at $\varpi = 30r_s$ was measured by integrating the accretion rate in the equatorial region $|z| < 5r_s$. The unit of the mass accretion rate is $\dot{M}_0 = 2\pi\rho_b r_s^2 c$. The mass-accretion rate at $\varpi = 2.5r_s$ becomes quasi-steady after about 10 rotational periods at the initial density maximum. The increase in the mass-accretion rate saturates when $\dot{M} \sim 0.3\dot{M}_0$. Mass accretion takes place due to efficient angular-momentum transport by Maxwell stress in an MRI-driven turbulent field. The equatorial mass-accretion rate at $\varpi = 30r_s$ shows a time variation with a timescale of $\sim 4000t_0$. Figure 1c shows the time evolution of the mass-outflow rate measured at $z = 40r_s$, computed by

$$\dot{M}_{out} = \int_2^{43} \int_0^{2\pi} \rho v_z \varpi \, d\varphi \, d\varpi \ .$$
(11)

The mass-outflow rate correlates with the mass-accretion rate with a time lag of about $4000t_0$.

Figure 2a shows the correlation between the mass-accretion rate at $\varpi = 2.5r_s$ and the mass-outflow rate measured at $z = 40r_s$ for model HT. The correlation was computed by

$$F(\delta t) = \int_{t_s}^{t_e} [(A(t) - \bar{A}) \cdot (B(t + \delta t) - \bar{B})]dt \ .$$
(12)

Here, $\bar{A}$ and $\bar{B}$ were averaged during the interval $t_s < t < t_e$. In figure 2, we adopted $t_s = 18000t_0$ and $t_e = 25000t_0$. The correlation function has peaks at $\delta t = 3400t_0$ and $\delta t = 4800t_0$. The mass-outflow rate at $z = 40r_s$ correlates with the mass-accretion rate at $\varpi = 2.5r_s$ with a delay of $3000t_0$–$5000t_0$. This timescale is comparable to that of the propagation time of the outflow, whose average speed is $\sim 0.01c$. Figure 2b shows the self-correlation function of the mass outflow rate at $z = 40r_s$ in the time interval $21500 < t/t_0 < 33500$. In addition to the
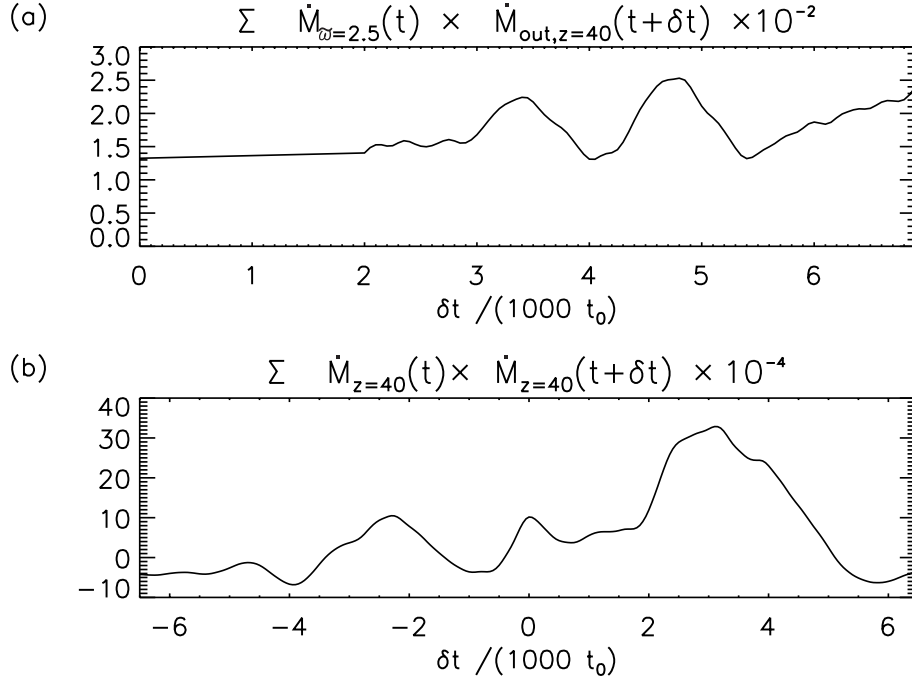
(a)

$$\Sigma \quad \dot{M}_{\varpi=2.5}(t) \times \dot{M}_{out,z=40}(t+\delta t) \times 10^{-2}$$

$\delta t \ /(1000 \ t_0)$

(b)

$$\Sigma \quad \dot{M}_{z=40}(t) \times \dot{M}_{z=40}(t+\delta t) \times 10^{-4}$$

$\delta t \ /(1000 \ t_0)$

Fig. 2. (a) Correlation between the mass accretion rate at $\varpi = 2.5 r_s$ and the mass outflow rate at $z = 40 r_s$. (b) Self correlation of the mass outflow rate at $z = 40 r_s$.
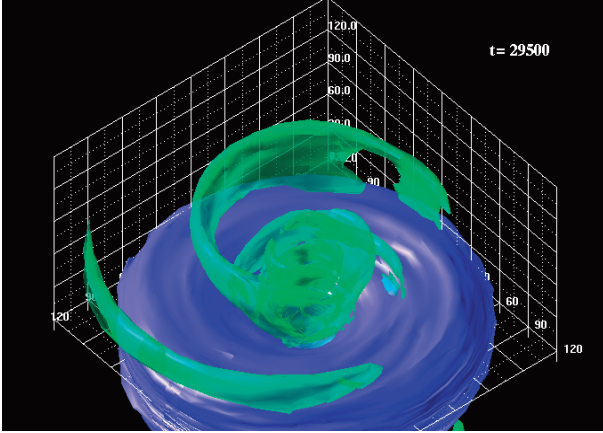
Fig. 3. Emergence of outflows from the inner region of the disk. Blue surfaces show the isosurface of the density ($\rho = 0.2$) for model HT at $t = 29500 t_0$. Green surfaces show the isosurface of the vertical velocity ($v_z = 0.05 \, c$).

peak at $\delta t = 0$, positive peaks appear around $\delta t = -2400 t_0$ and $\delta t = 2400 t_0$. This indicates that the mass-outflow rate oscillates quasi-periodically with a period of $\sim 2400 t_0$.

Figure 3 shows the isosurface of the density and the vertical velocity. Blue surfaces and green surfaces depict the density isosurface ($\rho = 0.2$) and the isosurface of the vertical velocity ($v_z = 0.05c$), respectively. Winds emerge intermittently from the inner region of the accretion disk. Toroidal magnetic fields are dominant in the wind. The intermittent ejection is driven by the expansion of magnetic loops anchored to the accretion disk (Kato et al. 2004).

Figure 4a shows the time evolution of the magnetic energy integrated in $4 < \varpi/r_s < 10$, and $|z|/r_s < 1$ normalized by the initial gas pressure at $(\varpi, z) = (\varpi_b, 0)$. Figure 4b shows the time evolution of $B_\varpi^2/8\pi$ averaged in $4 < \varpi/r_s < 10$, and $|z|/r_s < 1$. Figures 4c and 4d show the time evolution of $\alpha \equiv \langle B_\varpi B_\varphi/4\pi \rangle/\langle P \rangle$ and the ratio of the gas pressure to the magnetic pressure, $\beta \equiv P_{gas}/P_{mag}$, respectively. Although the magnetic energy decreases, the plasma β is nearly constant ($\beta \sim 8$) because the gas pressure also decreases. The fluctuations of the magnetic energy and the radial magnetic field correlate with the mass-accretion rate.

3.2. A Cool Accretion Disk: Model LT

Figure 5a shows the time evolution of the mass-accretion rate for model LT measured at $\varpi = 2.5 r_s$. Figure 5b shows the mass-accretion rate at $\varpi = 2.5 r_s$ (black) and the equatorial mass-accretion rate at $\varpi = 30 r_s$ (gray), which enlarges the time range $53000 < t/t_0 < 70000$. Figure 5c shows the time evolution of the mass-outflow rate measured at $z = 40 r_s$. In figure 5a, $\dot{M} \sim 0.04 \dot{M}_0$ is an order of magnitude smaller than that for model HT. This result indicates that the angular momentum transport rate strongly depends on the temperature of the gas supplied from the outer region.

Figure 6a shows the correlation between the mass-accretion rate at $\varpi = 2.5 r_s$ and the mass-outflow rate at $z = 40 r_s$ in the interval $52000 < t/t_0 < 62000$ for model LT. The mass-outflow rate correlates with the mass-accretion rate with a time delay of $5000 t_0$–$6000 t_0$. Figure 6b shows the self correlation of the mass-outflow rate at $z = 40 r_s$ in the interval $56650 < t/t_0 < 68650$. Positive peaks appear at $\delta t/t_0 = -1500, 0, 2400, 3500$, and 4700. It indicates that the mass-outflow rate oscillates with a period of $1000 t_0$–$2000 t_0$.
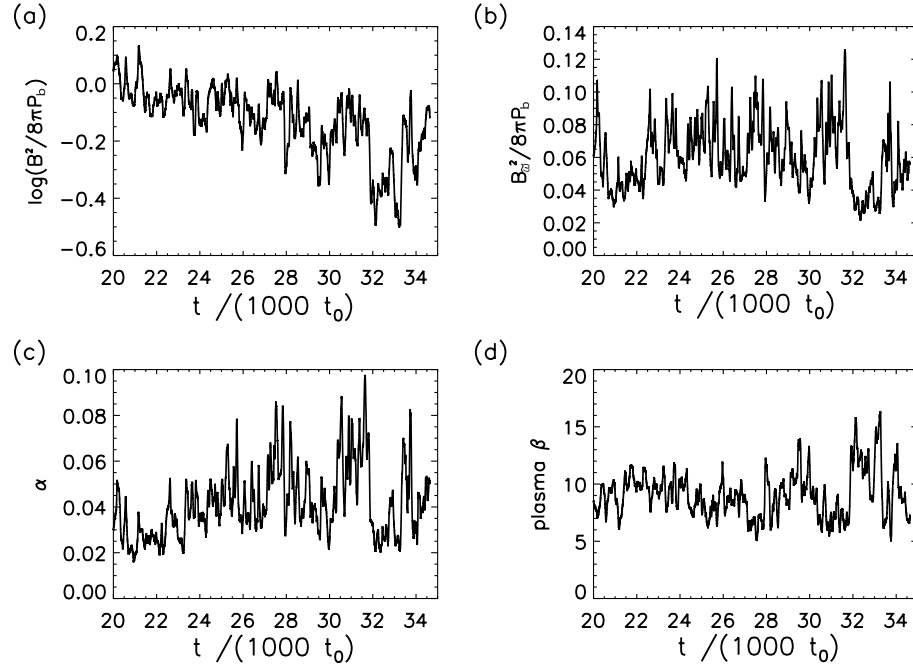
Fig. 4. Time evolution of physical quantities for model HT averaged in $4 < \varpi/r_s < 10$, $|z|/r_s < 1$, and $0 \le \varphi \le 2\pi$. (a) Magnetic energy, (b) $\langle B_\varpi^2/8\pi \rangle/P_b$, (c) time evolution of angular momentum transport rate, and (d) time evolution of the plasma β.
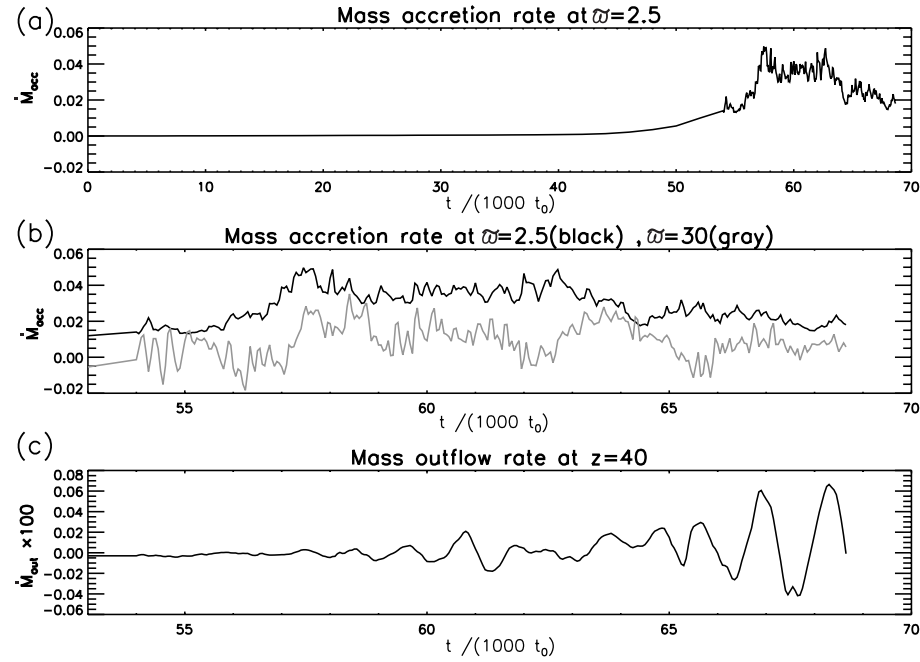

Fig. 5. (a) Time development of the mass-accretion rate, $\dot{M}$, at $\varpi = 2.5r_s$ for model LT. (b) Time evolution of the mass-accretion rate $\dot{M}$ at $\varpi = 2.5r_s$ (black) and the equatorial mass-accretion rate at $\varpi = 30r_s$ (gray). The interval $53000 < t/t_0 < 70000$ is enlarged. (c) Mass-outflow rate at $z = 40r_s$ for model LT.
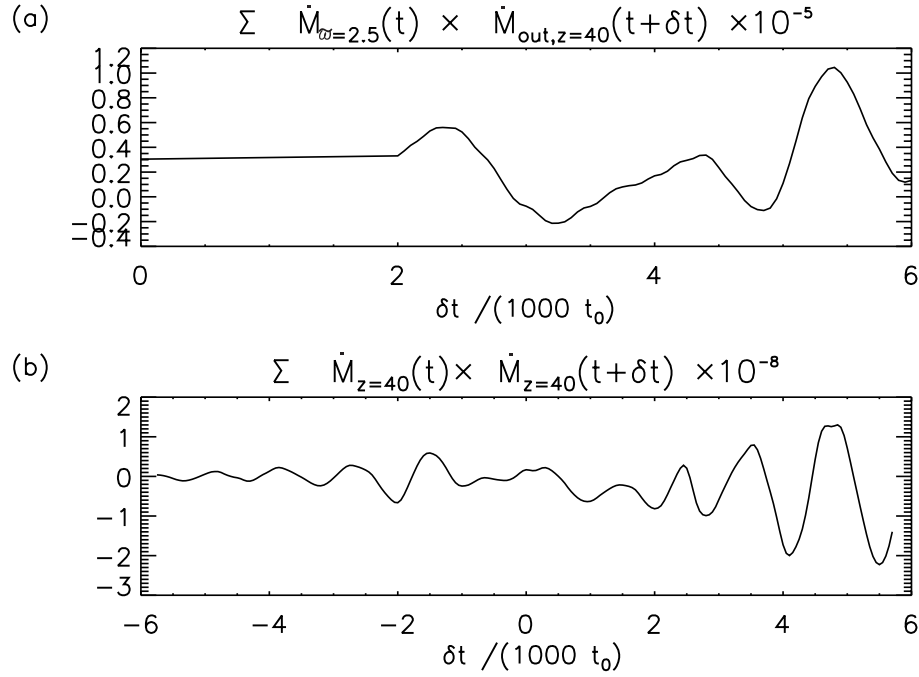
(a)

$$\Sigma \quad \dot{M}_{\varpi=2.5}(t) \times \dot{M}_{out,z=40}(t+\delta t) \times 10^{-5}$$

$\delta t \, /(1000 \, t_0)$

(b)

$$\Sigma \quad \dot{M}_{z=40}(t) \times \dot{M}_{z=40}(t+\delta t) \times 10^{-8}$$

$\delta t \, /(1000 \, t_0)$

Fig. 6. (a) Correlation between the mass-accretion rate at $\varpi = 2.5r_s$ and mass-outflow rate at $z = 40r_s$. (b) Self correlation of the mass outflow rate at $z = 40r_s$.
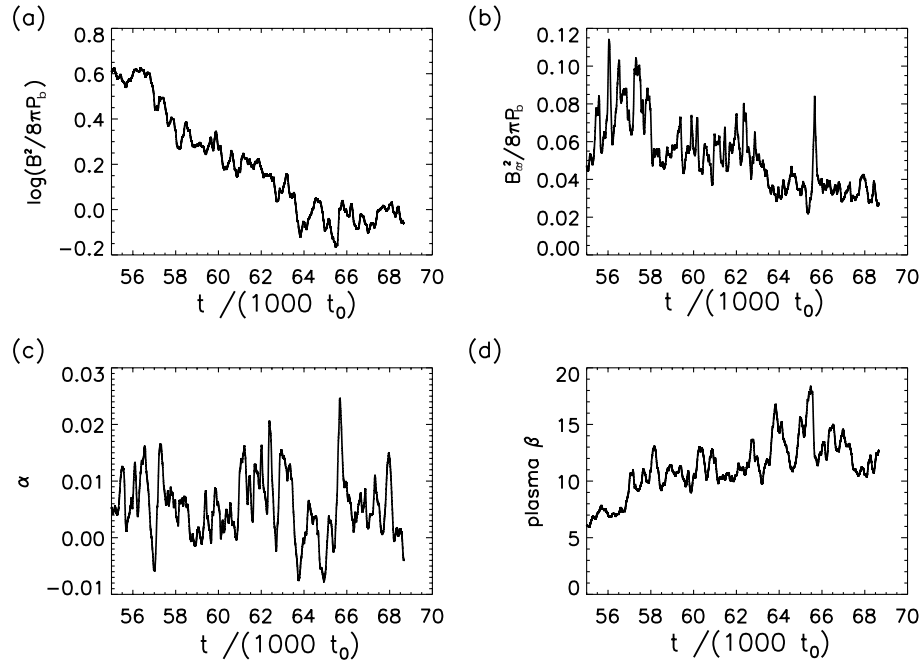
(a) $\log(B^2/8\pi P_b)$ — $t /(1000 \, t_0)$

(b) $B_{\varpi}^2/8\pi P_b$ — $t /(1000 \, t_0)$

(c) α — $t /(1000 \, t_0)$

(d) plasma β — $t /(1000 \, t_0)$

Fig. 7. Time evolution of (a) magnetic energy, (b) radial magnetic field, (c) angular momentum transport rate and (d) plasma β for model LT.
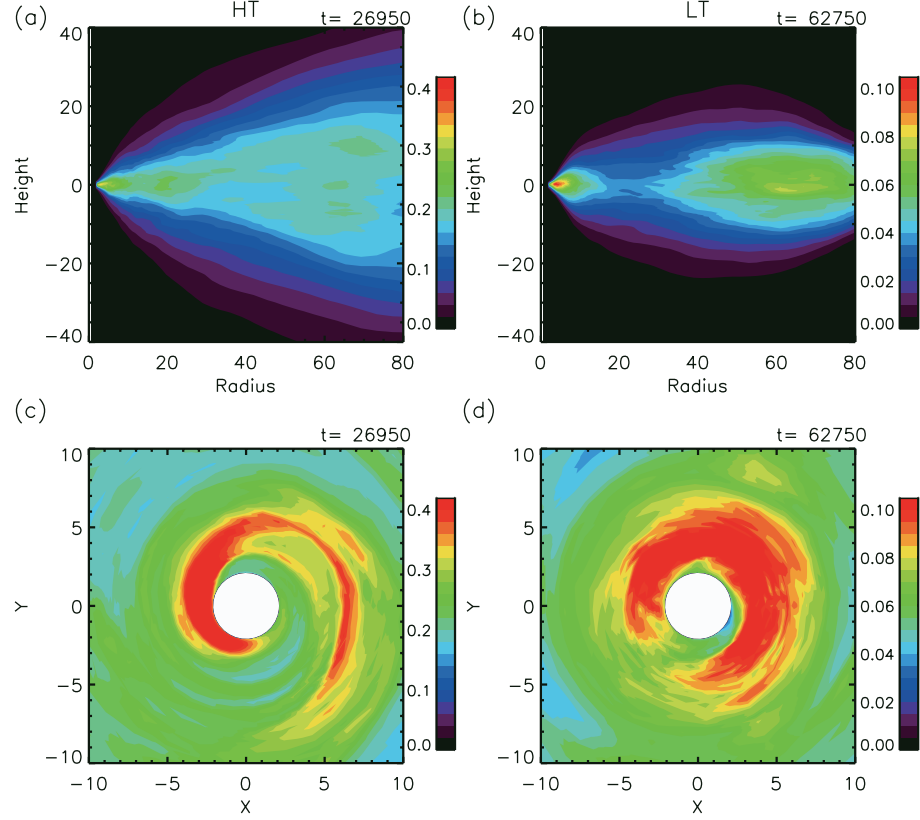
Fig. 8. Snapshots of the density distribution for model HT (left) and model LT (right). (a) and (b) show the density distribution averaged in the azimuthal direction. (c) and (d) show the density averaged in $|z|/r_s < 1$.

Figure 7 shows the time evolution of (a) magnetic energy, (b) $\langle B_\varpi^2/8\pi \rangle / P_b$, (c) the angular momentum transport rate α, and (d) the plasma β for model LT. The magnetic energy is averaged in the region $4 < \varpi/r_s < 10$, $|z/r_s| < 1$, and $0 \le \varphi \le 2\pi$. The magnetic energy gradually decreases when $t > 55000 t_0$. Figure 7c shows that $\alpha \sim 0.01$ in model LT. Since the magnetic energy decreases, the plasma β increases and stays around $\beta \sim 10$. Physical quantities shown in figure 7 show short time scale oscillations and longer time scale ($\sim 4000 t_0$) time variations. The latter is due to the time variation of the mass-accretion rate from the outer region.

4. Formation of an Inner Torus and its Oscillations

Figure 8 shows snap shots of the density distribution. Figures 8a and 8b show the density distribution in ϖ–z plane for model HT and LT, respectively. The density is averaged in the azimuthal direction. Figures 8c and 8d show the density distribution in the ϖ–φ plane averaged in $|z|/r_s < 1$. In model LT, an inner torus is created around $\varpi/r_s \sim 4$–8. The inner torus is deformed into a crescent-like shape. The inner torus is formed because angular-momentum transport becomes inefficient. Figures 7a and 7b indicate that Maxwell stress decreases due to a decrease in the magnetic energy. The magnetic energy decreases partly because the magnetic flux is swallowed into the black hole with accreting gas, and partly because the magnetic energy dissipates by magnetic reconnection. The deformation of a inner torus into a crescent

shape takes place due to the growth of the Papaloizou–Pringle instability (Papaloizou & Pringle 1984; Drury 1985).

When the disk is hot, since an inner torus is not formed, disk gas accretes to the black hole through dense, spiral channels (figure 8c). This result is consistent with a result obtained by simulations of the hot disk reported by Machida and Matsumoto (2003).

Figure 9 shows the time-averaged radial distribution of the physical quantities. The black curves show the results for model HT averaged in $23000 < t/t_0 < 29000$. The gray curve shows the result for model LT averaged in $55000 < t/t_0 < 61000$. Figure 9a displays the specific angular-momentum distribution. The dotted curve shows the Keplerian specific angular momentum using a pseudo-Newtonian potential. Since the angular momentum continuously decreases in model HT, no inner torus is formed in this model. In model LT (dashed curve), since α is small, nearly constant angular momentum inner torus is formed in $\varpi/r_s \sim 4$–8.

Figure 9b shows the radial distribution of $\alpha \equiv \langle B_\varpi B_\varphi / 4\pi \rangle / \langle P \rangle$. Inside the inner torus, the angular-momentum transport rate becomes very small. The solid and dashed curves in figure 9c show the sound speed and the Alfvén speed, respectively. Figure 9d shows the radial velocity. The accretion proceeds subsonically in $\varpi > 3 r_s$. In model LT, the accretion speed becomes very low in the inner torus.

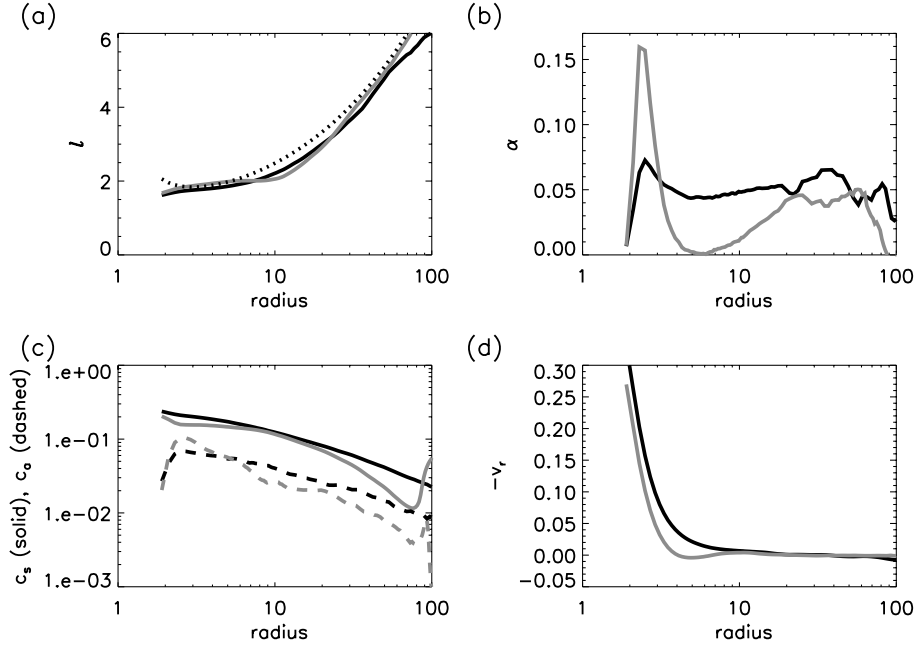Figure 10 shows the distribution of the azimuthally averaged temperature (10a, 10b), and the vertical velocity (10c,

Fig. 9. Radial distribution of physical quantities averaged in $|z|/r_s < 1$ and in the azimuthal direction. Black curves show the distribution for model HT averaged in $23000 < t/t_0 < 29000$. Gray curves show the distribution for model LT averaged in $55000 < t/t_0 < 61000$. (a) Time-averaged specific angular momentum distribution. The dotted curve shows the Keplerian specific angular momentum using a Pseudo-Newtonian potential. (b) Radial distribution of the angular momentum transport rate defined by $\alpha \equiv \langle B_\varpi B_\varphi/4\pi \rangle / \langle P \rangle$. (c) Solid curves and dashed curves show the sound speed and Alfvén speed, respectively. (d) Distribution of the radial velocity.

10d). Figures 10a and 10b show that accreting matter is significantly heated up. Figures 10c and 10d show that mass outflow emerges from the disk with an average speed of $0.01c$. The outflow is anti-symmetric to the equatorial plane. The outflow is more powerful in model HT. By comparing figures 8a and 10a, we can distinguish three regions; an equatorial disk, a hot funnel near the rotation axis, and outflows between the disk and the funnel. Accretion proceeds in the equatorial disk. A fraction of the accreting matter is ejected from the inner region of the disk.

Figure 11 shows the distribution of the azimuthal magnetic field (color) and magnetic fields depicted from the poloidal components of magnetic fields averaged in the azimuthal direction (curves). The azimuthal magnetic field is antisymmetric to the equatorial plane at this stage ($t = 26950t_0$ for model HT and $t = 62750t_0$ for model LT). Magnetic fields are turbulent inside the disk, but show more coherent structures in the interface between the disk and the halo, where mass outflow takes place. Magnetic field lines are stretched along this interface. A large-scale poloidal magnetic field is created in the funnel near the rotation axis.

Figure 12 shows snapshots of the density distribution on the $\varpi - \varphi$ plane for model LT. The density is averaged in the same region as that in figures 8c and 8d. The inner torus deforms its shape from a circle into a crescent, and from a crescent into a circle, repeatedly.

The top panel of figure 13 plots the time evolution of the ratio of the Joule-heating rate to the magnetic energy

averaged in $4 < \varpi/r_s < 10$, $|z|/r_s < 1$, and $0 \le \varphi \le 2\pi$. The ratio increases when magnetic energy is released (when $\langle B^2/8\pi \rangle$ decreases or ηJ^2 increases). The ratio changes quasi-periodically with a time scale of $\sim 1000t_0$.

The bottom panel of figure 13 shows the time evolution of the amplitude of non-axisymmetric $m = 1$ mode (m is the mode number in the azimuthal direction) of the density. The amplitude of the azimuthal mode is computed by Fourier decomposing the density contrast,

$$\rho/\langle\rho\rangle = \rho / \int_{2.9}^{5.3} \int_{-1}^{1} \rho \, d\varpi dz \ . \tag{13}$$

The running average of the amplitude is plotted using the amplitude during $250t_0$ for each point. The gray curve depicts the same curve as that in figure 13. The amplitude of the $m = 1$ mode anti-correlates with $\eta J^2/\langle B^2/8\pi \rangle$. This indicates that the magnetic energy is released when the $m = 1$ mode disappears. The amplitude of the $m = 1$ mode also correlates with $\langle B_\varpi^2 \rangle$ (figure 7b) and α (figure 7c). They all show long timescale ($t \sim 4000t_0$) variation and short timescale ($t \sim 1000t_0$) oscillations. The peaks of the short timescale oscillations in the Fourier amplitude of the $m = 1$ mode in figure 13 coincide with those in figure 7.

Figure 14 shows the mass-accretion rate measured at $\varpi = 4r_s$ (black), magnetic energy (gray), and the Fourier amplitude of the $m = 1$ mode for the density (dashed) for model LT. When the magnetic energy increases inside the inner torus, the mass-accretion rate increases because the angular-
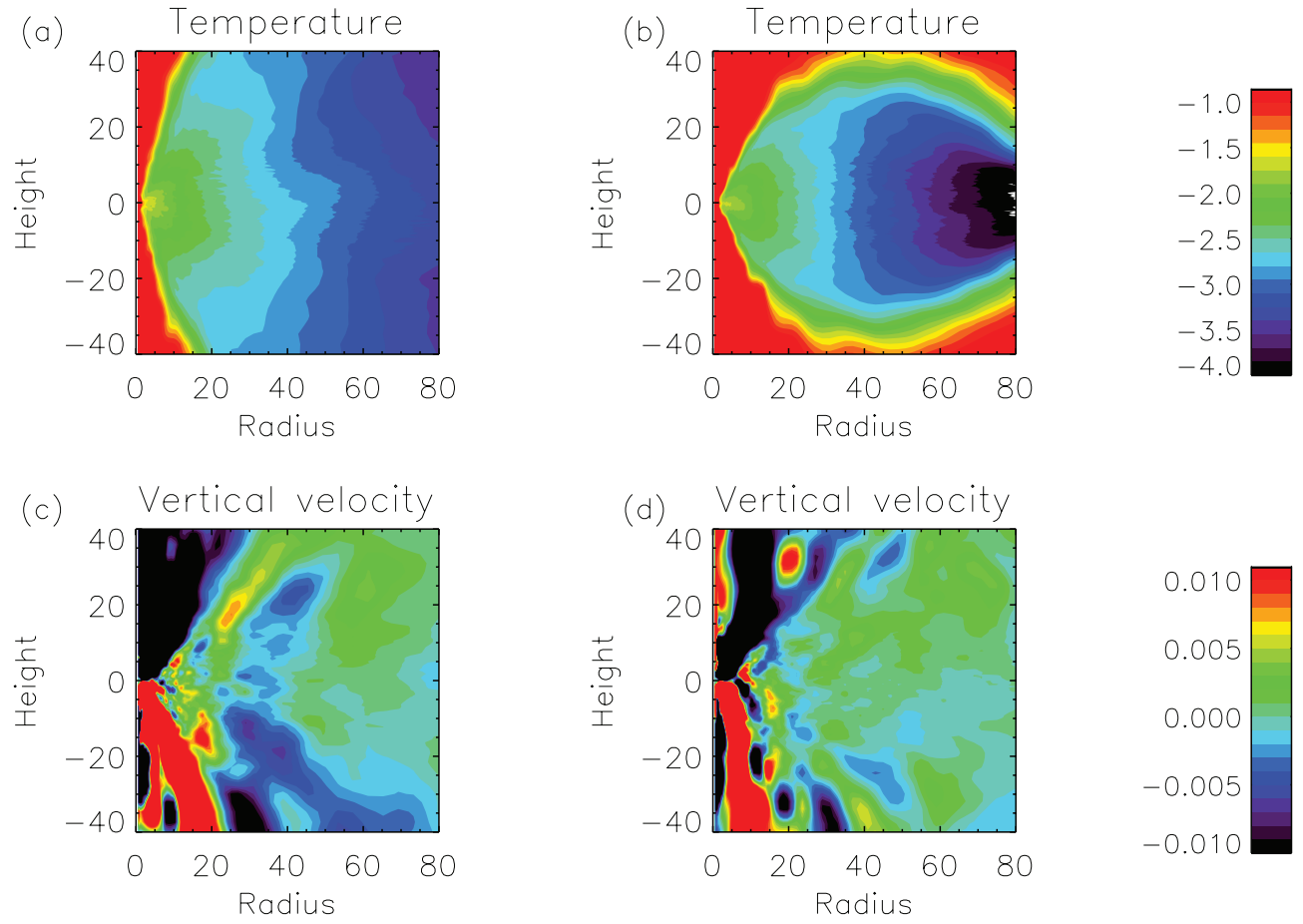
Fig. 10. (a) and (b) $\varpi - z$ slice of distribution of temperature $\log(T/T_0)$ averaged in the azimuthal direction. (c) and (d) distribution of the vertical velocity averaged in the azimuthal direction. (a) and (c) are at $t = 26950 t_0$ for model HT, and (b) and (d) are at $t = 62750 t_0$ for model LT.
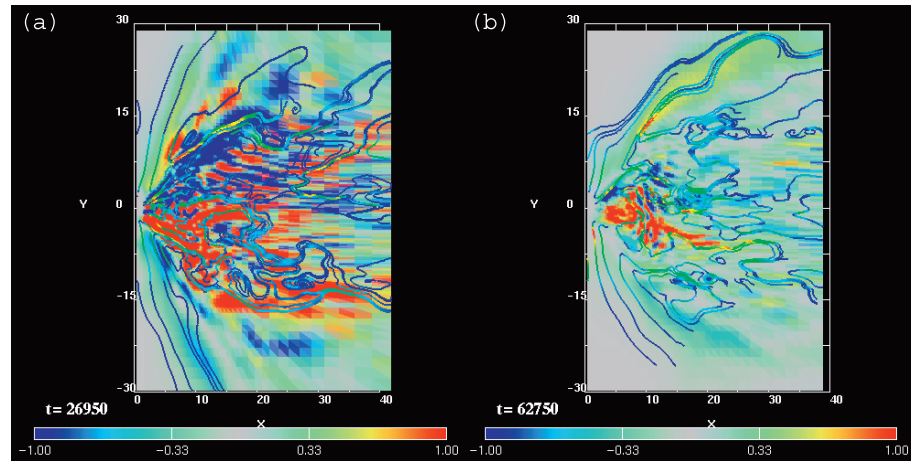

Fig. 11. Distribution of azimuthal magnetic field (color) and magnetic field lines (blue curves). The magnetic field lines are depicted from the poloidal components of magnetic fields averaged in the azimuthal direction. (a) model HT and (b) model LT .
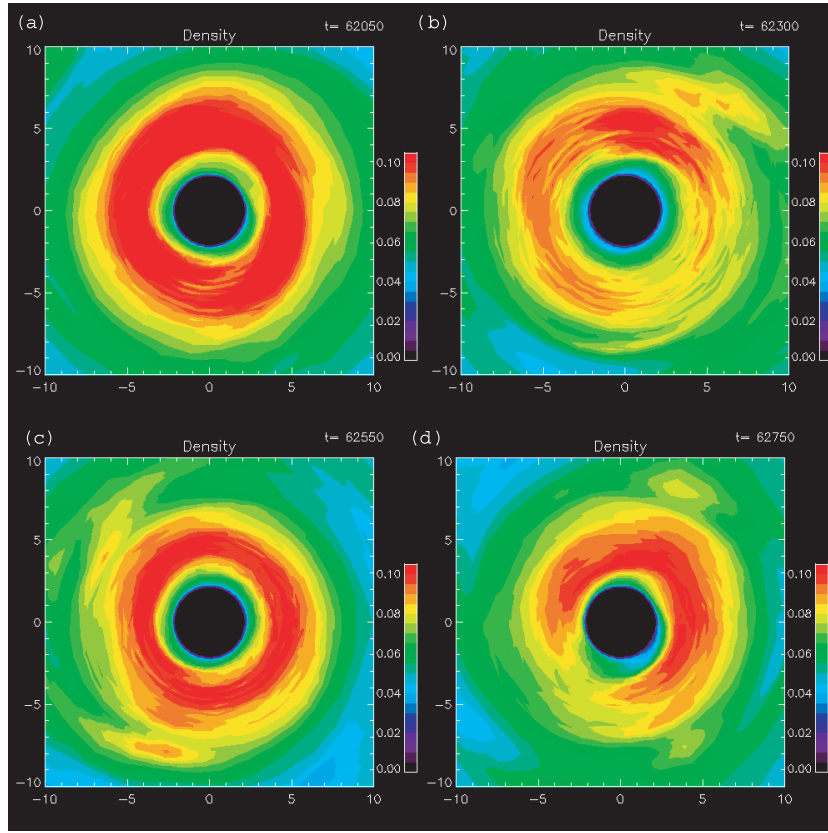
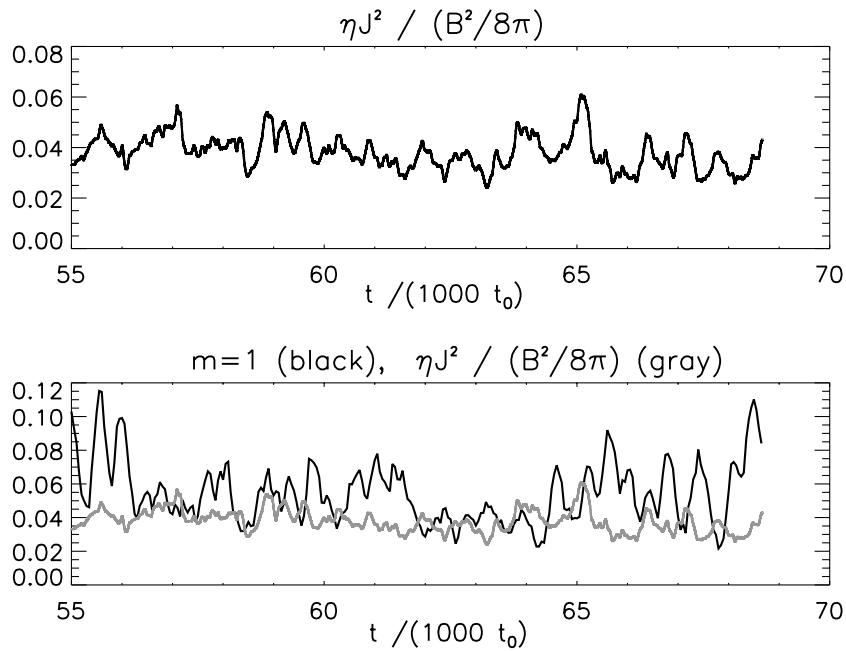**Fig. 12.** Snapshots of the density distribution on the $\varpi-\varphi$ plane for model LT.

Fig. 13. (top) Time evolution of the ratio of the Joule-heating rate to the magnetic energy for model LT. (bottom) Time evolution of the Fourier amplitude of the non-axisymmetric mode with the azimuthal mode number $m=1$ computed from the density distribution (black). The gray curve depicts the same curve as that in the top panel.

momentum transport rate increases as magnetic energy (and magnetic stress) is accumulated in the torus. On the other hand, when the magnetic energy is released, the mass accretion rate decreases. The amplitude of the $m = 1$ mode (dashed curve in figure 14) correlates with the magnetic energy (gray). The magnetic fields are amplified when the amplitude of the $m = 1$ mode increases. On the other hand, the amplitude of the $m = 1$
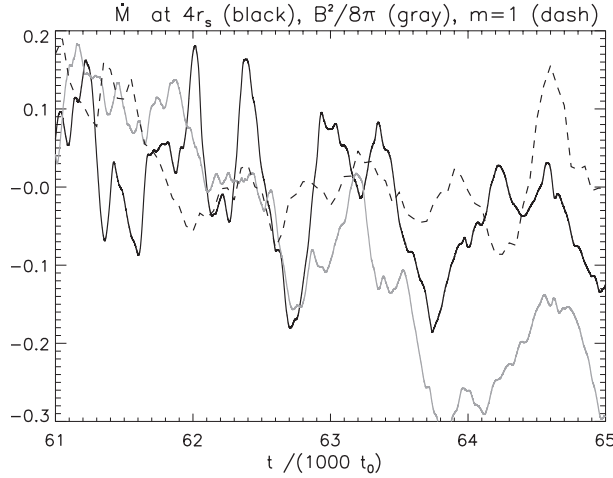
mode decreases when the magnetic energy is released. When the Maxwell stress decreases due to a decrease in the magnetic energy, the Papaloizou–Pringle instability grows again inside the torus. Therefore, the torus deforms itself into a crescent shape. The interval between magnetic energy releases in the inner torus is $\sim 1000 t_0$.

Figure 15a shows the correlation between the amplitude of the $m = 1$ mode and the Joule-heating rate normalized by the magnetic energy for model HT. The correlation function has positive peaks at $\delta t / t_0 = -2500$, 0, and 3000. The positive correlation at $\delta t = 0$ indicates that magnetic energy is released when a $m = 1$ spiral channel (see figure 8c) develops. This result is consistent with that reported in Machida and Matsumoto (2003), where we showed that magnetic reconnection takes place in the spiral channel. Other peaks in the correlation function indicate that the $m = 1$ mode develops quasi-periodically with an interval of 2500–3000 t_0.

Figure 15b shows the correlation between the amplitude of the $m = 1$ mode and the Joule-heating rate for model LT. In contrast to that in model HT, no positive peak appears at $\delta t = 0$. Instead, a negative peak appears at $\delta t / t_0 = -1200$ and positive peaks appear at $\delta t / t_0 = 1200, 2400$. This indicates that the $m = 1$ mode anti-correlates with the Joule-heating rate, and that the growth of the $m = 1$ mode precedes a release of magnetic energy by $\delta t \sim 1200 t_0$.

Figure 16 shows the spatial distribution of the Fourier amplitude, νP_ν, of time variabilities in the mass-accretion rate for model HT in $23000 < t / t_0 < 32000$, and for model LT in $55000 < t / t_0 < 64000$. In model HT, various peaks appear at various radius. On the other hand, in model LT, low-frequency QPOs around 10 Hz appear in $5 < \varpi / r_s < 10$, where the inner torus is formed.
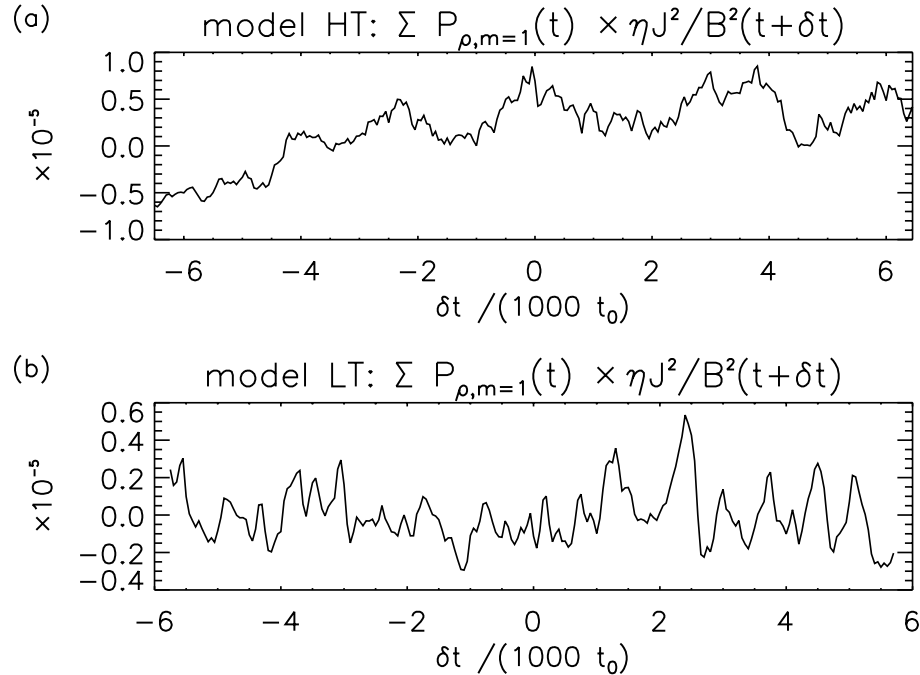

Fig. 14. Correlation of the time evolution of the mass-accretion rate and magnetic energy in model LT. (black) Time evolution of the mass accretion rate measured at $\varpi = 4 r_s$. (gray) Time evolution of the magnetic energy integrated in $4 < \varpi / r_s < 10$, $|z| / r_s < 1$, and $0 \le \varphi \le 2\pi$. (dashed) Fourier amplitude of the $m = 1$ mode in the density distribution. The curves are arbitrarily shifted in the vertical direction.

Fig. 15. Correlation function between the amplitude of the $m = 1$ mode and the Joule-heating rate normalized by the magnetic energy. (a) is model HT and (b) shows model LT.
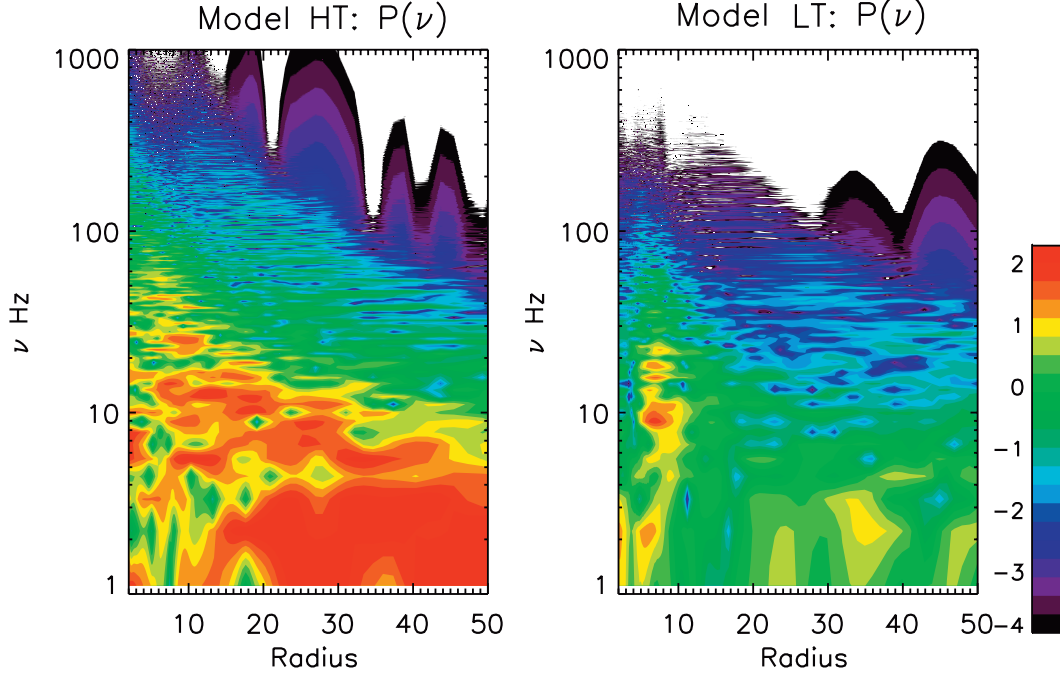
Fig. 16. Radial distribution of the Power Spectral Density (PSD) of the time variation of the mass-accretion rate for model HT measured in $23000 < t/t_0 < 32000$ (left) and for model LT measured in $55000 < t/t_0 < 64000$ (right).
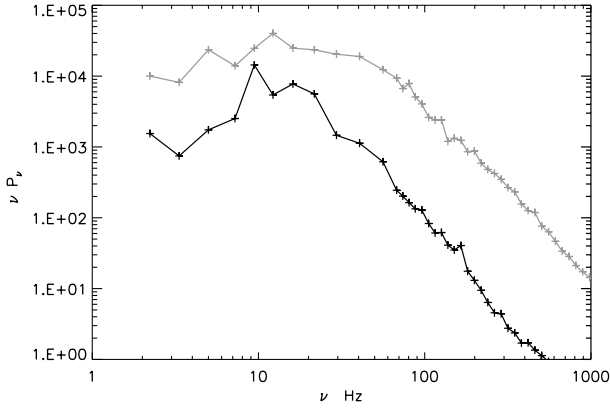

Fig. 17. Power spectrum, νP_ν, where P_ν is the Fourier power of the time variation of the mass-accretion rate averaged in $2.5 < \varpi/r_s < 29$ and $|z|/r_s < 1$ for model LT (black) and for model HT (gray).

Figure 17 shows the Power Spectral Density (PSD) of the time variation of the mass-accretion rate averaged in $3 < \varpi/r_s < 8$ and $|z|/r_s < 1$. Black and gray curves show PSD (νP_ν where P_ν is the Fourier power) for model LT and model HT, respectively. We adapted the data in the time range $23000 < t/t_0 < 32000$ in model HT and $55000 < t/t_0 < 64000$ in model LT.

The PSD for model LT has a broad low-frequency peak around 10 Hz. This low-frequency peak corresponds to the oscillation involving the amplification and release of magnetic energy in the inner torus. The PSD for model HT is flat in $\nu \le 10$ Hz, which means that $P_\nu \propto \nu^{-1}$, and changes its slope around $\nu \sim 50$ Hz. Since oscillations are excited at various

radius in model HT, PSD shows a flat spectrum. The PSD in model LT has a slope steeper than that in model HT in $30\,\mathrm{Hz} < \nu < 100\,\mathrm{Hz}$.

In model LT in figure 17, a small peak appears at $\nu \sim 150$ Hz. Based on a simulation using 32 azimuthal grid points, Matsumoto and Machida (2007) pointed out that a high-frequency QPO appears when the disk shows low-frequency (~ 8 Hz) sawtooth-like oscillations of magnetic energy. Here, we confirmed that low-frequency QPOs and high-frequency QPOs coexist by a simulation including twice as many grid points in the azimuthal direction.

5. Discussion

In this paper, we considered the dependence of the structure and time variation of black-hole accretion flows on the gas temperature supplied from the outer region. When hot gas ($T \sim 10^{10}$ K) is supplied, the angular momentum is transported efficiently all the way to the black hole. The average ratio of the Maxwell stress to the gas pressure, $\alpha \equiv \langle B_\varpi B_\varphi/4\pi\rangle/\langle P\rangle \sim 0.05$, is consistent with previous simulations by Hawley (2001) and Machida and Matsumoto (2003). Such disks correspond to the radiatively inefficient, optically thin disk in the low/hard state of black-hole candidates. Our simulation clearly showed the appearance of outflows with a maximum speed of $\sim 0.05c$ from such hot disks. The mass outflow rate, $\dot{M}_{out}$, is comparable to the mass-accretion rate to the black hole. The magnetic fields are turbulent inside the disk, but they show large-scale coherent structures near to the rotation axis. Plasma flows out in the interface between the funnel and the accretion disk. The hot accretion flow shows time variations whose PSD is flat in $\nu \le 10$ Hz when the mass

of the central black hole is $M \sim 10 M_{\odot}$.

When a cool plasma is supplied, an inner torus is formed around $\varpi \sim 4$–$8 r_{\rm s}$. Such a torus is formed when the MRI-generated turbulent magnetic field is dissipated inside the disk. Since Maxwell stress decreases due to the decrease of magnetic energy, α decreases to $\alpha \leq 0.01$. Thus, a nearly constant-angular-momentum torus is formed in the innermost region ($\varpi < 10 r_{\rm s}$) of the accretion flow. We found that the inner torus deforms itself into a crescent shape. Such a deformation takes place due to the growth of a non-axisymmetric instability in geometrically thick tori (Papaloizou & Pringle 1984).

Such a non-axisymmetric structure enhances the growth of MRI. As the magnetic energy increases, the angular-momentum transport rate increases. Thus, the accretion rate increases. When the magnetic energy accumulated in the disk is released, the disk comes back to being a weakly magnetized, axisymmetric torus. A new cycle begins as the magnetic energy is amplified by MRI. The period of the cycle is about $1000 t_0$ in model LT. It creates a low-frequency peak around 4–8 Hz in the PSD of the mass accretion rate. Low-frequency QPOs, sometimes observed in a low/hard state and a hard intermediate state (HIMS) of black-hole candidates can be reproduced by such magnetic cycles. We also showed that a high-frequency QPO is excited when a low-frequency QPO appears.

Let us discuss why the magnetic cycle is excited when low-temperature gas is supplied. When hot gas accretes, since the scale height of the gas is large, large eddies are formed in the magnetically turbulent disk, which create a large-scale coherent magnetic field that transports angular momentum efficiently. On the other hand, when low-temperature gas is supplied, since the scale height and eddy size become smaller, angular momentum is transported only in the local region. Thus, the angular momentum is transported more efficiently in high-temperature disks.

Low-temperature plasmas can be supplied when a cooling instability takes place in the outer disk. Machida et al. (2006) carried out a global 3D MHD simulation of black-hole accretion flows by including radiative cooling. They showed that when the density of the outer disk is sufficiently high, a cooling instability takes place. The outer disk shrinks vertically, and forms a magnetically supported, cool, optically thin disk. When such cool plasma accretes, the magnetic cycle may be excited in the inner region.

The amplitude of the $m = 1$ non-axisymmetric mode correlates positively with the Joule-heating rate in model HT, but anti-correlates in model LT. In model HT, since the angular momentum transport rate is large enough, mass smoothly accretes along the spiral channel, in which the magnetic fields are stretched, and form a current sheet. Magnetic energy is released in such current sheets. Therefore, the amplitude of the $m = 1$ mode correlates with the Joule-heating rate. On the other hand, in model LT, non-axisymmetric $m = 1$ pattern disappears when the magnetic energy is released.

Homan et al. (2005) pointed out that during the transition from the LHS to HSS, GX339−4 shows a sub-transition from HIMS dominated by power-law X-ray radiation to a soft inter-mediated state (SIMS) dominated by radiation from an optically thick disk. They also showed that low-frequency QPOs appear when the X-ray spectrum stays in HIMS and SIMS, and sometimes in LHS. The high-frequency QPOs appear in the HIMS and SIMS. When the high-frequency QPO is observed, a low-frequency QPO is always observed in the X-ray spectrum. This tendency is consistent with our simulation results.

A number of theoretical models have been proposed for high-frequency QPOs. Abramowicz and Kulźniak (2001) proposed that high-frequency QPOs are formed by the resonance of radial and vertical oscillations. Kato (2001a) studied the excitation of high-frequency QPOs by resonance with the disk warp. In our simulation, a high-frequency peak appears around $\nu \sim 150$ Hz when the low-frequency oscillation is prominent. In our simulation, however, the low-frequency oscillation was weakened due to heating of the inner torus. We expect that when the extra heating is extracted by radiative cooling, the magnetic cycle may continue, and excite high-frequency QPOs. We would like to report the results of numerical simulations, including radiative cooling, in subsequent papers.

In this work, we treated the relativistic effect by using a pseudo-Newtonian potential. The accuracy of this approximation is worst near the black hole's horizon, especially for spinning black holes. When we include the effects of black-hole spin, the inner torus will be formed closer to the black hole. Thus, higher frequency QPOs will appear due to oscillation of the inner torus. We should note that the disk luminosity depends on relativistic beaming and light bending. In subsequent papers, we would like to report PSDs obtained by relativistic ray-tracing of numerical results.

References

Abramowicz, M. A., & Kulźniak, W. 2001, A&A, 374, L19

Belloni, T., et al. 2006, MNRAS, 367, 1113

Di Matteo, T., & Psaltis, D. 1999, ApJ, 526, L101

Drury, L. O'C. 1985, MNRAS, 217, 821

Gallo, E., Fender, R. P., & Pooley, G. G. 2003, MNRAS, 344, 60

Hawley, J. F. 2001, ApJ, 554, 534

Homan, J., Buxton, M., Markoff, S., Bailyn, C. D., Nespoli, E., & Belloni, T. 2005, ApJ, 624, 295

Homan, J., & Belloni, T. 2005, in From X-ray Binaries to Quasars: Black Holes on All Mass Scales, ed. T. J. Maccarone, R. P. Fender, & L. C. Ho (Dordrecht: Springer), 107

Ichimaru, S. 1977, ApJ, 214, 840

Kato, S. 2001a, PASJ, 53, 1

Kato, S. 2001b, PASJ, 53, L37

Kato, S. 2004, PASJ, 56, 905

Kato, Y. 2004, PASJ, 56, 931

Kato, Y., Mineshige, S., & Shibata, K. 2004, ApJ, 605, 307

Kawaguchi, T., Mineshige, S., Machida, M., Matsumoto, R., & Shibata, K. 2000, PASJ, 52, L1

Machida, M., & Matsumoto, R. 2003, ApJ, 585, 429

Machida, M., Nakamura, K. E., & Matsumoto, R. 2006, PASJ, 58, 193

Matsumoto, R., & Machida, M. 2007, in IAU Symp. 238, Black Holes from Stars to Galaxies, eds. V. Karas & G. Matt, (Cambridge: Cambridge University Press), 37

McClintock, J. E., & Remillard, R. A. 2006, in Compact Stellar X-ray Sources, eds, W. H. G. Lewin & M. van der Klis (Cambridge: Cambridge Univ. Press), Chap. 4

Narayan, R., & Yi, I. 1994, ApJ, 428, L13

Narayan, R., & Yi, I. 1995, ApJ, 444, 231

Negoro, H., Kitamoto, S., Takeuchi, M., & Mineshige, S. 1995, ApJ, 452, L49

Oda, H., Machida, M., Nakamura, K. E., & Matsumoto, R. 2007, PASJ, 59, 457

Okada, R., Fukue, J., & Matsumoto, R. 1989, PASJ, 41, 133

Paczyński, B., & Wiita, P. J. 1980, A&A, 88, 23

Papaloizou, J. C. B., & Pringle, J. E. 1984, MNRAS, 208, 721

Richtmyer, R. D., & Morton, K. W. 1967, Difference Methods for Initial-Value Problems, 2nd ed. (New York: Interscience Publishers), Chap. 13

Rubin, E. L., & Burstein, S. Z. 1967, J. Comp. Phys., 2, 178

Shaposhnikov, N., Swank, J., Shrader, C. R., Rupen, M., Beckmann, V., Markwardt, C. B., & Smith, D. A. 2007, ApJ, 655, 434

Yokoyama, T., & Shibata, K. 1994, ApJ, 436, L197